

Cite this: *J. Mater. Chem.*, 2011, **21**, 11486

www.rsc.org/materials

COMMUNICATION

Size-dependent CO₂ capture in chemically synthesized magnesium oxide nanocrystals†‡Anne M. Ruminski,^a Ki-Joon Jeon^{§b} and Jeffrey J. Urban^a

Received 23rd April 2011, Accepted 26th May 2011

DOI: 10.1039/c1jm11784j

The carbon dioxide storage capacity of magnesium oxide (MgO) particles was examined as a function of particle size, shape, and surface area. Two types of MgO nanocrystals (5 nm spheres and 23 nm disks) were synthesized and compared against commercially available MgO (325 mesh/44 µm and 40 mesh/420 µm). The surface area of the four types of particles was determined by N₂ gas adsorption. Carbon dioxide capture was measured at 60 °C and 600 °C using thermogravimetric analysis, with results indicating enhanced CO₂ capacity correlating with increased surface area.

Compelling evidence suggests that anthropogenic carbon dioxide (CO₂) emissions are a leading cause of global warming, thus there exists an urgent need to develop methods for CO₂ mitigation.¹ Currently, a primary focus is on carbon capture from power plant flue streams and the subsequent sequestration of captured CO₂. Consequently, materials for carbon capture have recently received great attention. These materials include metal–organic frameworks,² metal–organic gels,³ zeolitic imidazolate frameworks,⁴ porous polymer networks,⁵ and steel slag oxides.⁶ While many of these materials reversibly bind CO₂, which is desirable for transient carbon capture and subsequent carrier looping, metal oxides (*e.g.* CaO, MgO, *etc.* found in steel slag) are an attractive entity for both carbon capture and long-term CO₂ fixation. Chemically, CO₂ reacts with metal oxides to form thermodynamically stable solid metal carbonates (*e.g.* MgCO₃, $\Delta H_f \approx 1100 \text{ kJ mol}^{-1}$). At room temperature, gaseous CO₂ adsorbs to metal oxides by physisorption (reversible) and/or chemisorption (irreversible).⁷ Recent reports indicate that high-density CO₂ adsorption on metal oxides is possible by chemisorption at elevated temperatures,⁸ although the exact dependence of this rate on particle size, shape, and surface chemistry remains largely unknown. Chemical transformations of nanomaterials can exhibit increased kinetics relative to their parent bulk solids due to their high surface area to

volume ratio and resulting short diffusion paths.⁹ Similarly, the increased surface area to volume ratio of nanomaterials provides more available surface area for CO₂ interactions than a corresponding mass of bulk material, thus allowing for larger CO₂ adsorption density. In this communication, we examine the CO₂ adsorption capacity of magnesium oxide nanocrystals as a function of size, shape, and surface area. We show that the process can be reversible, which is a necessary characteristic for potential CO₂ capture looping applications.

In order to explore the dependence of CO₂ sorption on surface area to volume ratio, a number of uniform MgO samples ranging in size were required. Here, to maximize the range of surface area to volume ratio (SA/V) of the magnesium oxide (MgO) crystals studied, we utilized chemical synthesis to produce MgO nanocrystals and compared them to commercially available micron-sized MgO crystalline powders. This provides a $\sim 90\,000 : 1$ range in surface area to volume ratio for analysis.

Using a synthesis developed by our group,¹⁰ MgO nanocrystals averaging 2.5 nm in diameter ($d_{\text{avg}} \approx 5 \text{ nm}$ in diameter post-heat treatment, 1.2 SA/V) were prepared (MgO-NP1). Briefly, bis(cyclopentadienyl) magnesium (Cp₂Mg, 308 mg, 2 mmol), dried triethylphosphine oxide surfactant (TOPO, 80 mg, 0.2 mmol) and 20 µL deionized water were rapidly stirred in distilled benzyl ether (4 mL) at 285 °C for 2 h under an inert atmosphere. After cooling to room temperature, methanol was added to the reaction solution followed by centrifugation to precipitate and clean the nanocrystals, followed by subsequent separation and collection.

A second MgO nanocrystalline sample (MgO-NP2) consisting of larger nanoparticles was synthesized by adaptation of a two-step reaction developed for iron oxide nanocrystals (Fe₃O₄).¹¹ MgO nanodisks with a diameter of roughly 43 nm ($\sim 23 \text{ nm}$ post-heat treatment, 0.26 SA/V) were produced by first combining magnesium chloride hexahydrate (2.033 g, 10 mmol) with sodium oleate (9.134 g, 30 mmol) in ethanol (20 mL), deionized water (15 mL), and hexane (35 mL). The solution was refluxed at 70 °C for 4 h to form a magnesium oleate complex. After cooling to room temperature, the top organic layer was separated, rinsed 3× with deionized water, and placed under vacuum overnight to dry. Next, dry magnesium oleate (1.174 g, 2 mmol) was combined with oleic acid surfactant (0.281 g, 1 mmol) and distilled water (50 µL) in triethylamine (10 g). The solution was heated at a rate of 3.3 °C min^{-1} to 365 °C, and kept at 365 °C for 30 min. After cooling to room temperature, ethanol was added to the solution to flocculate the nanocrystals, which were subsequently separated by centrifugation.

^aThe Molecular Foundry, Material Science Division, Lawrence Berkeley National Laboratory, Berkeley, CA, 94720, USA. E-mail: jjurban@lbl.gov

^bEnvironmental Energy Technologies Division, Lawrence Berkeley National Laboratory, Berkeley, CA, 94720, USA

† This paper is part of a Journal of Materials Chemistry theme issue on the chemical transformations of nanoparticles.

‡ Electronic supplementary information (ESI) available. See DOI: 10.1039/c1jm11784j

§ Present address: School of Electrical Engineering, University of Ulsan, Ulsan 680-749, Republic of Korea.

In order to study a broad range of surface area to volume ratios, two commercially available micron-sized magnesium oxide particles were also examined in comparison to the MgO nanocrystal samples. The materials are denoted by mesh size, and are herein labeled as

MgO-325M (325 mesh, 44 μm , $\sim 1.4 \times 10^{-4}$ SA/V) and MgO-40M (40 mesh, 420 μm , $\sim 1.4 \times 10^{-5}$ SA/V).

The commercially purchased material was 99.5% and 98.5% pure MgO-325M and MgO-40M, respectively. Chemically synthesized nanoparticles are typically surrounded by a surfactant ligand which stabilizes the particle, preventing agglomeration and providing chemical stability. However, these surfactant ligands greatly reduce the purity of the material on a per mass basis—in some cases 50% of the overall sample mass is attributed to the ligand. In the following section, we perform a detailed analysis of the ligand–nanocrystal interactions, and ultimately remove all ligands to facilitate comparisons between the chemically derived MgO nanocrystals and ligand-free micron-sized MgO samples.

As details of nanocrystal surface chemistry can greatly impact chemical interactions, the surface chemistry of each of the nanocrystals was examined through attenuated total reflectance Fourier transform infrared spectroscopy (ATR-FTIR, Fig. 1A). Spectra of the nanocrystals displayed peaks characteristic of the surfactant and reaction solvent. MgO-NP1 featured peaks representing the presence of aromatic C–H stretching bonds at 3030–3090 cm^{-1} (benzyl ether) and methylene C–H stretching bonds at 2850–2930 cm^{-1} (TOPO and benzyl ether). The MgO-NP2

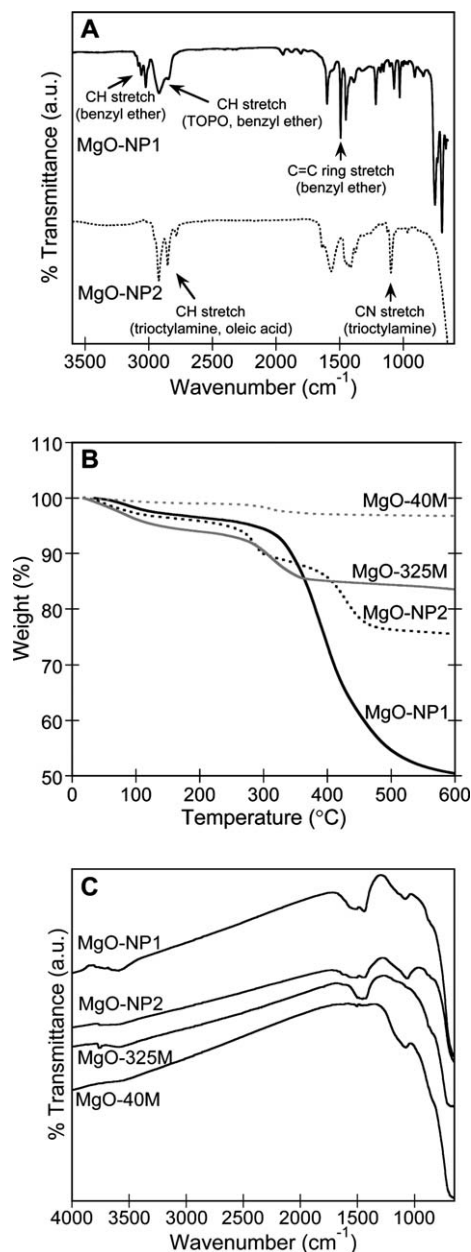


Fig. 1 (A) Attenuated total reflectance Fourier transform infrared (ATR-FTIR) spectroscopy of chemically synthesized MgO nanocrystals, (top) MgO-NP1 and (bottom) MgO-NP2. Prominent peaks corresponding to surfactant ligands are labeled. (B) Thermogravimetric analysis performed at a heating rate of 5 $^{\circ}\text{C min}^{-1}$ on the four MgO samples: MgO-NP1 (black solid line), MgO-NP2 (black dotted line), MgO-325M (grey solid line) and MgO-40M (grey dotted line). (C) Transmission FTIR analysis of heat-treated MgO: (top to bottom) MgO-NP1, MgO-NP2, MgO-325M and MgO-40M. Spectra have been offset for clarity. Heat-treated MgO powdered samples were pressed into pellets in KBr followed by heating at 550 $^{\circ}\text{C}$ under nitrogen for 1 h.

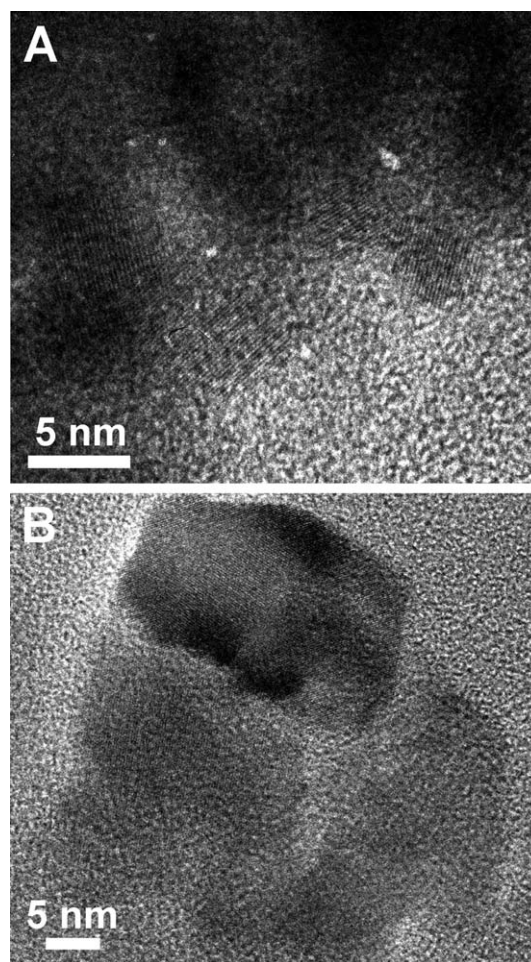


Fig. 2 Transmission electron microscope (TEM) images of heat-treated MgO: (A) MgO-NP1, mean particle diameter is 5 \pm 1 nm. (B) MgO-NP2, mean particle diameter is 23 \pm 8 nm.

spectrum displayed a C–N stretch band at 1097 cm^{-1} (trioctylamine) and methylene C–H stretching bands at $2775\text{--}2925\text{ cm}^{-1}$ (trioctylamine and oleic acid).

Furthermore, the extent of surface ligand coverage on each nanocrystal system was characterized by thermogravimetric analysis (TGA, Fig. 1B). Increased temperature exposure of the nanocrystals in an inert nitrogen atmosphere causes desorption of surface ligands without any chemical transformation. Results indicate that MgO-NP1 and MgO-NP2 are composed of 49.4 and 24.3 weight% ligand, respectively. For comparison, TGA of the two commercial mesh MgO samples gave a considerably smaller weight% loss (3.2 and 16.3% for MgO-40M and MgO-325M, respectively, Fig. 1B). Weight loss of the bare commercial MgO is attributed to the removal of physisorbed water and dehydration of trace $\text{Mg}(\text{OH})_2$.

In order to more accurately compare the CO_2 adsorption ability of the four magnesium oxide particle sizes, all materials were subjected to a preconditioning heat treatment to remove surface ligands and any physisorbed water. This ensures that all crystalline surfaces studied were as uniform as possible, thus eliminating differences in surface chemistry from obfuscating our conclusions. Samples were heated in air at a rate of 5°C min^{-1} to 600°C , and kept at 600°C for 1 h. Transmission FTIR spectra of powdered samples pelleted in KBr after heat treatment did not show signs of organic material (Fig. 1C). The presence of broad bands between 1250 and 1650 cm^{-1} indicated the existence of bulk-like carbonate species, while the broad band at 3590 cm^{-1} (O–H stretching) indicated adsorbed water.^{12,13}

Transmission electron microscopy (TEM) was performed to examine the morphology and size of the synthesized nanocrystals

(ESI, Fig. S1†). Before the heat treatment, MgO-NP1 images displayed particles spherical in shape with a size distribution of $2.5 \pm 0.5\text{ nm}$. After heat treatment, MgO-NP1 was $5 \pm 1\text{ nm}$ in diameter (Fig. 2). Images of as synthesized MgO-NP2 revealed thin nanodisks of MgO ranging from $32\text{--}53\text{ nm}$ across in both circular and rectangular shapes. Lattice fringes were visible in atomic resolution TEM (ESI, Fig. S2†) for MgO-NP2, and are consistent with MgO-NP2 being best described as thin plates or sheets. TEM images of MgO-NP2 post-heat treatment revealed thin sheets ranging between 6 and 51 nm in diameter, having an average diameter of $23 \pm 8\text{ nm}$ (Fig. 2).

X-Ray diffraction analysis before and after a preconditioning heat treatment (ESI, Fig. S3†) confirms that both synthetic routes (MgO-NP1, MgO-NP2) produced cubic MgO (JCPDS 07-0239) that were not remarkably affected by the 600°C heat treatment. Debye–Scherrer peak analysis of MgO-NP1 spectra acquired before and after heat treatment indicated a nanoparticle diameter of $2.7 \pm 0.2\text{ nm}$ and $9 \pm 3\text{ nm}$, respectively. These values correspond well with diameters measured by TEM. The maximum diameter observed by TEM of heat-treated MgO-NP1 was 9 nm . The highly anisotropic shape of MgO-NP2 observed *via* TEM precludes straightforward XRD peak breadth analysis, although it does indicate that the average smallest lattice dimension in these samples is no less than $15 \pm 2\text{ nm}$ and $16.6 \pm 0.7\text{ nm}$ before and after heat treatment.

To assess the available surface area and pore structure of the heat-treated preconditioned samples, a simple geometric model based on size and density was used to determine the maximum surface area.

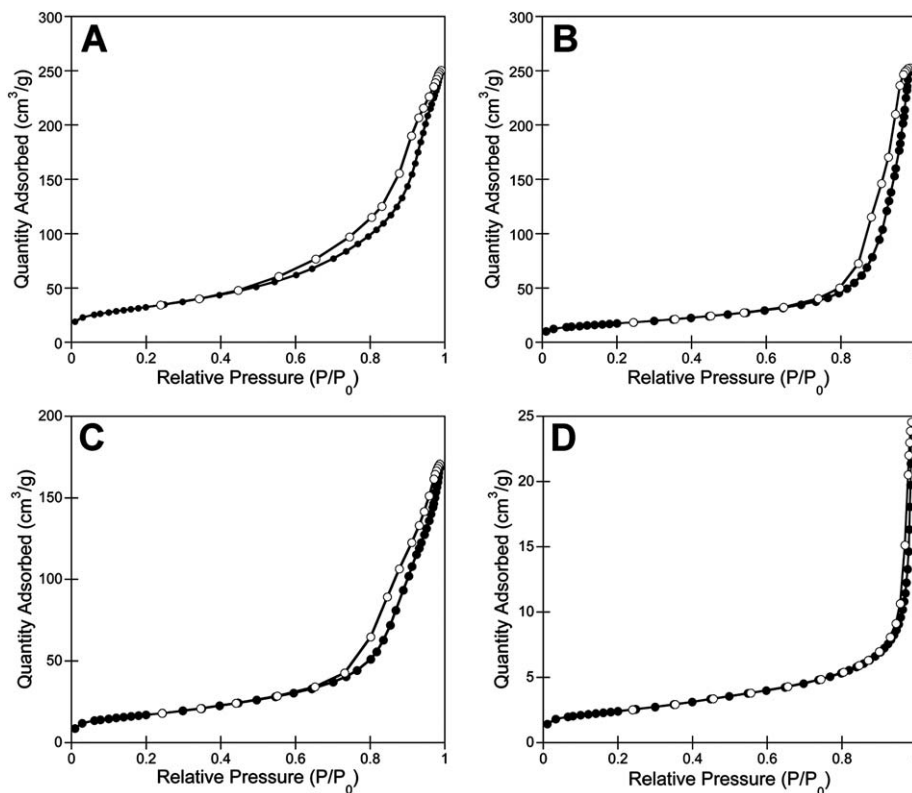


Fig. 3 N_2 adsorption (solid circles) and desorption (open circles) isotherms of heat-treated (A) MgO-NP1 (5 nm), (B) MgO-NP2 (23 nm), (C) MgO-325M ($44\text{ }\mu\text{m}$) and (D) MgO-40M ($420\text{ }\mu\text{m}$). Application of the Brunauer–Emmett–Teller theory yields surface areas of 116 , 62 , 61 and $8.5\text{ m}^2\text{ g}^{-1}$, respectively.

The calculated surface areas for the crystals were 335, 73, 3.8 and $0.40 \text{ m}^2 \text{ g}^{-1}$ for MgO-NP1, MgO-NP2, MgO-325M and MgO-40M, respectively. Additionally, N_2 gas adsorption/desorption isotherms were performed at 77 K (Fig. 3, ESI, Fig. S4†). All samples exhibit a Type IV isotherm (following the IUPAC 1985 classification of physisorption isotherms), characteristic of mesoporous samples with high affinity for the gases. These type IV isotherms contain a hysteresis loop with characteristic filling (lower branch) and emptying (upper branch) of mesopores by capillary condensation.¹⁴ The hysteresis loop, Type H3, is typical of aggregates of flat and broad particles or adsorbents containing slit-shaped pores. The MgO-NP1 data display hysteresis loop closure of the desorption branch at a relative pressure P/P_0 of 0.45. Forced closure at this pressure has been reported as a result of a tensile strength effect,¹⁵ which is characteristic behavior of the adsorptive material, and not the adsorbent. A clear size-dependent trend in the adsorption data was observed, as anticipated. The largest surface area determined by the Brunauer–Emmett–Teller method was obtained by MgO-NP1, at $116 \text{ m}^2 \text{ g}^{-1}$. For comparison, smaller silica particles of 2 nm diameter reported a monolayer N_2 adsorption BET surface area of $325 \text{ m}^2 \text{ g}^{-1}$.¹⁶ Unexpectedly, BET analysis indicated that the disk-like

nanocrystals MgO-NP2 possessed a similar surface area as the smallest mesh micron particles, MgO-325M, reporting values of 62 and $61 \text{ m}^2 \text{ g}^{-1}$, respectively. Scanning electron microscope (SEM) images of MgO-325M show polydisperse and agglomerated particles ranging from 200 nm to microns in size (ESI, Fig. S5†). Lastly, a surface area of $8.5 \text{ m}^2 \text{ g}^{-1}$ was yielded by MgO-40M. Polydisperse particles ranging from 1–20 μm across were observed by SEM for MgO-40M (ESI, Fig. S5†), thus rendering the measured surface area reasonable.

The CO_2 adsorption capacity of the four MgO materials was examined using thermogravimetric analysis (Fig. 4). A temperature of 60°C was chosen to mimic temperatures used in postcombustion capture from fuel gas processes.¹⁷ Samples (10 mg) were kept at a constant temperature of 60°C while the atmosphere was alternated between pure N_2 and pure CO_2 gas at a flow rate of 25 sccm. Results show appreciable CO_2 adsorption by 3 of the MgO materials: MgO-NP1, MgO-NP2 and MgO-325M. MgO-40M, which has the largest particle size and lowest surface area, did not measurably respond to CO_2 introduction. Weight% change upon CO_2 gas introduction was 0.7 ± 0.2 , 0.22 ± 0.04 , and $0.21 \pm 0.09\%$ for MgO-NP1, MgO-NP2 and MgO-325M, respectively. This response

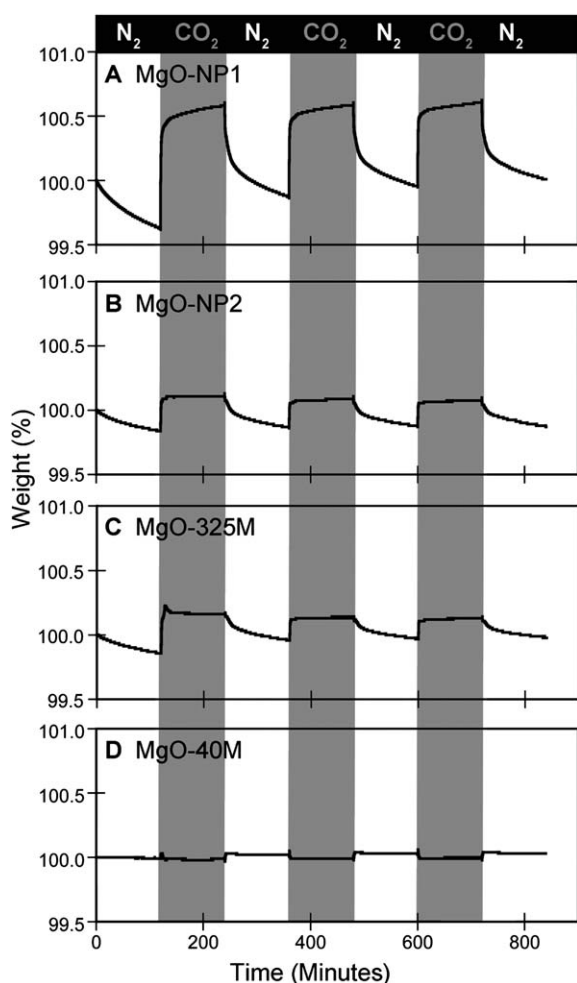


Fig. 4 Cycling of CO_2 gas adsorption (gray background) and desorption (by pure N_2 gas, white background) on heat-treated MgO at 60°C : (A) MgO-NP1 (5 nm), (B) MgO-NP2 (23 nm), (C) MgO-325M (44 μm) and (D) MgO-40M (420 μm).

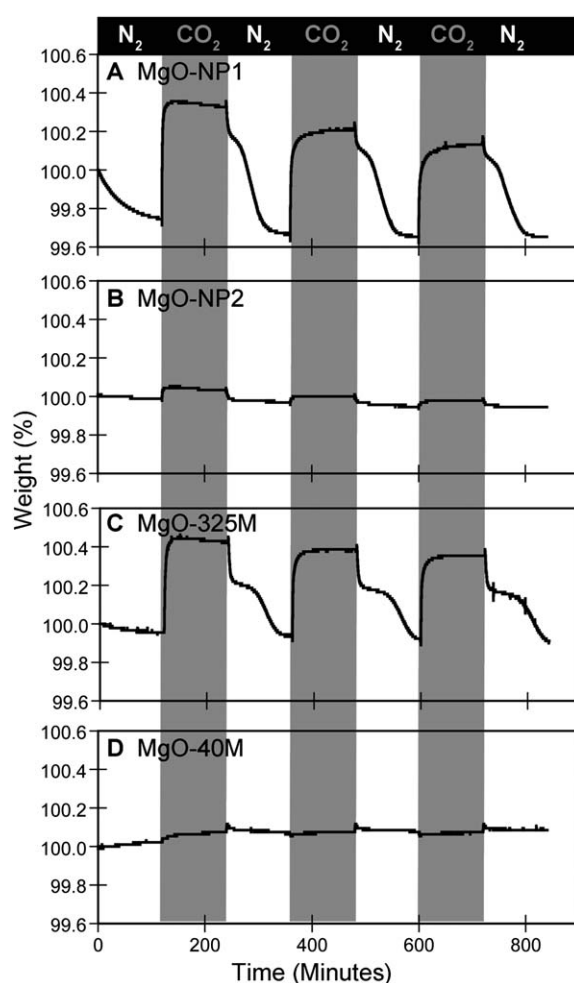


Fig. 5 600°C cycling of CO_2 gas adsorption (gray background) and desorption (by pure N_2 gas, white background) on heat-treated MgO: (A) MgO-NP1 (5 nm), (B) MgO-NP2 (23 nm), (C) MgO-325M (44 μm) and (D) MgO-40M (420 μm).

to CO₂ correlates with the BET measured surface areas: MgO-NP1 with the largest surface area had the largest weight% change with CO₂. Samples MgO-NP2 and MgO-325, which had the same measured surface area, also had the same change in weight% when exposed to CO₂. Gas adsorption was reversible and repeatable.

CO₂ exposure was repeated at a higher temperature of 600 °C (Fig. 5). In general, the MgO samples largely followed surface area trends, with a weight% change to CO₂ gas introduction averaging at $0.54 \pm 0.07\%$, $0.46 \pm 0.03\%$, and $0.04 \pm 0.01\%$ for MgO-NP1, MgO-325M, and MgO-NP2, respectively. The largest sample, MgO-40M, again displayed no measurable response to CO₂. At higher temperature and greater thermal energy, the nanocrystal samples displayed a lower weight% change to CO₂ gas in comparison to at 60 °C, while alternatively, MgO-325M experienced an increase in response. At this time we do not have definitive data explaining the enhanced response of MgO-325M, however the increased temperature exposure of 600 °C for many hours may have been a factor. For instance, it has been reported that at higher temperatures (1450 °C, bulk MgO) polar oxide surfaces are stabilized by surface reconstructions.¹⁸ Additionally, studies have shown that oxygen vacancies affect the surface reactivity of MgO, and are mobile at elevated temperatures (900 °C, bulk MgO).^{19,20} Moreover, SEM analysis of MgO-325M images taken after the preconditioning heat treatment *versus* images acquired after heating at 600 °C under nitrogen for 15 h (ESI, Fig. S6†) indicates that mobility of surface atoms, as indicated by grain growth and morphological changes, is producing large changes in the mesh samples.

One major difference between the measured CO₂ adsorption/desorption curves at the two temperatures is the appearance of a two-step desorption process for samples MgO-NP1 and MgO-325M at 600 °C. We propose that the first step displaying an abrupt weight% change is due to the quick removal of physisorbed CO₂ when the atmosphere is reverted back to pure N₂. The second step, with a gradual weight% change, could be attributed to the slower release of chemisorbed CO₂. To assess this possibility, FTIR spectra were recorded from all samples after exposure to CO₂ at 60 and 600 °C. To do so, CO₂ exposed MgO powders were quickly mixed with KBr and made into a pellet in laboratory atmosphere. Although *ex situ* spectra were taken promptly post-experiment, quantitative analysis of peak intensities during the absorption events cannot be made, however qualitative evidence of CO₂ binding was observed with all four samples. Characteristic bands with peaks at 1446 and 1490 cm⁻¹ may be assigned to monodentate carbonate species, 1543 cm⁻¹ to bicarbonate species, and 1595 cm⁻¹ to bidentate carbonate species.^{12,20,21} Crucially, no bands were observed at 2400–2200 cm⁻¹, indicative of the lack of physisorbed and end-on chemisorbed CO₂ species.¹³ These data further corroborate the docking and strong bonding of CO₂ with these nanocrystal surfaces.

At both temperatures, all samples reached 90% of weight change within 10 min of CO₂ exposure. The time required for desorption was longer at 60 °C, typically requiring 2 h or more. At 600 °C, full desorption was achieved within 2 h, and within 10 min for MgO-NP2. These are reasonable bounds (90% weight change in 10 min) for parameter optimization in a CO₂ looping scheme.

The CO₂ carrying capacity of MgO materials in the form of complete conversion to MgCO₃ is 44 g CO₂ per 40.3 g MgO, or 109 weight%. The materials reported here carried between 0.04 and 0.7 weight%, and hence need to be greatly enhanced to reach full CO₂ carrying capacity. However, these initial studies on size and surface

area effect on CO₂ adsorption produce some insight into metal oxide to metal carbonate conversion, indicating that even in nanocrystalline systems the uncatalyzed rates of formation remain sluggish at room temperature and low pressures. The fact that the adsorption tracks well with surface area indicates that the full conversion capacity of MgO can be realized in open frameworks of this structure, such as metal-organic frameworks or zeolites.

In summary, we demonstrate the enhancement of CO₂ adsorption capacity of metal oxides through the use of high surface area nano-scale materials. We observed a change in reactivity of MgO at 600 °C. In order to better understand this reactivity change, future work will be focused on examining how these changes vary with respect to specific crystal faces, steps, and grain boundaries. Additional efforts will be placed on further increasing the surface area through use of porogens and targeted acid treatments on these materials.

Acknowledgements

Work at the Molecular Foundry was supported by the Office of Science, Office of Basic Energy Sciences, at the U.S. Department of Energy under Contract No. DE-AC02-05CH11231. A.M.R. is supported as part of the Center for Nanoscale Control of Geologic CO₂, an Energy Frontier Research Center funded by the U.S. Department of Energy, Office of Science, Office of Basic Energy Sciences under Contract No. DE-AC02-05CH11231. K.J.J. is supported under B&R code KC0202020, Hydrogen Storage program.

Notes and references

- 1 IPCC, ed. B. Metz, O. Davidson, H. C. de Coninck, M. Loos and L. A. Meyer, 2005.
- 2 A. Demessence, D. M. D'Alessandro, M. L. Foo and J. R. Long, *J. Am. Chem. Soc.*, 2009, **131**, 8784–8786; D. Britt, H. Furukawa, B. Wang, T. G. Glover and O. M. Yaghi, *Proc. Natl. Acad. Sci. U. S. A.*, 2009, **106**, 20637–20640.
- 3 S. K. Nune, P. K. Thallapally and B. P. McGrail, *J. Mater. Chem.*, 2010, **20**, 7623–7625.
- 4 A. Phan, C. J. Doonan, F. J. Uribe-Romo, C. B. Knobler, M. O'Keeffe and O. M. Yaghi, *Acc. Chem. Res.*, 2010, **43**, 58–67.
- 5 H.-S. Choi and M. P. Suh, *Angew. Chem., Int. Ed.*, 2009, **48**, 6865–6869.
- 6 D. Bonenfant, L. Kharoune, S. Sauvé, R. Hausler, P. Niquette, M. Mimeault and M. Kharoune, *Int. J. Greenhouse Gas Control*, 2009, **3**, 20–28.
- 7 M. Bhagiyalakshmi, J. Y. Lee and H. T. Jang, *Int. J. Greenhouse Gas Control*, 2010, **4**, 51–56.
- 8 H.-K. Song, K. Won Cho and K.-H. Lee, *J. Non-Cryst. Solids*, 1998, **242**, 69–80.
- 9 J. Graetz and J. J. Reilly, *Adv. Eng. Mater.*, 2005, **7**, 597–601; D. H. Son, S. M. Hughes, Y. Yin and A. P. Alivisatos, *Science*, 2004, **306**, 1009–1012; A. Zaluska, L. Zaluski and J. O. Ström-Olsen, *Appl. Phys. A: Mater. Sci. Process.*, 2001, **72**, 157–165.
- 10 H. R. Moon, J. J. Urban and D. J. Milliron, *Angew. Chem., Int. Ed.*, 2009, **48**, 6278–6281.
- 11 J. Park, K. An, Y. Hwang, J.-G. Park, H.-J. Noh, J.-Y. Kim, J.-H. Park, N.-M. Hwang and T. Hyeon, *Nat. Mater.*, 2004, **3**, 891–895.
- 12 J. Hu, K. Zhu, L. Chen, C. Kübel and R. Richards, *J. Phys. Chem. C*, 2007, **111**, 12038–12044.
- 13 G. A. H. Mekhemer, S. A. Halawy, M. A. Mohamed and M. I. Zaki, *J. Phys. Chem. B*, 2004, **108**, 13379–13386.
- 14 F. Rouquerol, J. Rouquerol and K. Sing, *Adsorption by Powders and Porous Solids*, Academic Press, London, 1999.

-
- 15 L. Vradman, M. V. Landau, D. Kantorovich, Y. Koltypin and A. Gedanken, *Microporous Mesoporous Mater.*, 2005, **79**, 307–318.
- 16 V. Rabolli, L. C. J. Thomassen, C. Princen, D. Napierska, L. Gonzalez, M. Kirsch-Volders, P. H. Hoet, F. Huaux, C. E. A. Kirschhock, J. A. Martens and D. Lison, *Nanotoxicology*, 2010, **4**, 307–318.
- 17 D. M. D'Alessandro, B. Smit and J. R. Long, *Angew. Chem., Int. Ed.*, 2010, **49**, 6058–6082.
- 18 M. Gajdardziska-Josifovska, R. Plass, M. A. Schofield, D. R. Giese and R. Sharma, *J. Electron Microsc.*, 2002, **51**, S13–S25.
- 19 T. König, G. H. Simon, U. Martinez, L. Giordano, G. Pacchioni, M. Heyde and H.-J. Freund, *ACS Nano*, 2010, **4**, 2510–2514.
- 20 J. V. Stark, D. G. Park, I. Lagadic and K. J. Klabunde, *Chem. Mater.*, 1996, **8**, 1904–1912.
- 21 R. Philipp and K. Fujimoto, *J. Phys. Chem.*, 1992, **96**, 9035–9038.